Electronic and x-ray-absorption structure in compressed copper

R. C. Albers
Materials Science and Technology Division, Los Alamos National Laboratory, Los Alamos, New Mexico 87545

A. K. McMahan
Lawrence Livermore National Laboratory, Livermore, California 94550

J. E. Müller
Institut für Festkörperforschung der Kernforschungsanläge Jülich, D-5170 Jülich, West Germany
(Received 16 July 1984)

Using electronic band-structure techniques, we calculate the K- and L-edge absorption spectra for fcc copper over a wide range of compressions. As copper is compressed the x-ray-absorption structure greatly increases and copper deviates more and more from its normal-density free-electron-like behavior. We explain this additional structure in terms of an increased scattering amplitude with pressure and relate it to both extended x-ray-absorption fine-structure (EXAFS) theory and a simple Friedel-model calculation. We show that specific band symmetry points can be well correlated with the x-ray-absorption near-edge structure features, but that this procedure is useless at higher energies above the edge (the EXAFS region). We suggest that the energy dependence of the peaks in the spectra can be used as a high-pressure volume diagnostic. We also discuss general complications and limitations in our knowledge about high-pressure x-ray-absorption spectra as well as overall changes in the electronic structure of copper under compression. To correlate our results with applied pressure, we also present zero-temperature equation-of-state calculations (pressure versus volume).

I. INTRODUCTION

In recent years, x-ray absorption has been increasingly used as an experimental probe of electronic structure in matter under high pressure. Static high-pressure cells and the availability of synchrotron-radiation sources, in addition to conventional x-ray sources, have made room-temperature investigations up to 0.33 Mbar possible.[1–5] Diamond-anvil cells[6] can achieve pressures approaching 1 Mbar, although x-ray-absorption measurements are then complicated by the Bragg scattering out of the beam from the diamond crystal planes.[2] Much bigger pressures can be obtained by dynamic methods, including a novel laser-driven technique that is currently being used to measure K-edge absorption structure in shock-compressed samples up to almost 30 Mbar.[7] These experiments can achieve nearly threefold compression, although with concomitant heating of the sample to temperatures on the order of 10 eV. Far more extreme conditions than these occur in inertial-confinement fusion targets, where the x-ray-emission rather than -absorption spectrum is of most interest as a diagnostic.[8]

There has also been considerable theoretical progress over the last five years in using the techniques of electron-band theory to calculate x-ray-absorption spectra for solids at normal conditions.[9–13] These calculations extend up to 100—200 eV above the absorption edge, covering the x-ray-absorption near-edge structure (XANES) region from 0 to 50 eV and some of the extended x-ray-absorption fine-structure (EXAFS) region[14] considered to range from 50 to 1000 eV above the absorption edge. Calculated K- and L-edge spectra for transition metals[9–11] and rare earths[12] have compared quite favorably with experiment.[13] To our knowledge, however, there has been no application of this approach to a systematic investigation of the pressure dependence of x-ray-absorption spectra in solids.

The present work reports electron-band-structure calculations of the volume and pressure dependence of K- and L-edge x-ray-absorption spectra for fcc copper, a material whose absorption spectrum at 1 atm has already been well studied, both experimentally[15–17,18] and theoretically.[10,18] As in previous work at 1 atm,[10] the present calculations extend in energy through the XANES into the EXAFS region. We have focused on the effects of zero-temperature compression, in order to understand first the far more tractable problem of cold, compressed matter before adding the complications introduced by thermal disorder at elevated temperatures. Nevertheless, our results are still relevant to compression techniques which do not substantially heat the sample. These include isothermal diamond-anvil compression, nearly isentropic techniques, and shock compression well before melt. It is important to note that thermal disorder, as indicated by the Debye-Waller factor, typically decreases in the course of both isothermal and isentropic compression.[19]

As already noted, diamond-anvil cells can achieve pressures approaching 1 Mbar, or about a compression of $V_0/V=1.4$ in the case of room-temperature Cu. While Cu melts at about a compression of $V_0/V=1.5$ under shock loading, quasi-isentropic techniques use multiple weak shocks to achieve high pressures with greatly re-

duced temperature increases. Multi-megabar pressures have been achieved in such experiments using both magnetic flux compression[20] and mechanical density-gradient impactor techniques.[21] The use of temporally shaped laser pulses to achieve near-isentropic compression has also been one of the original goals of the laser-fusion program,[22] and it has been recently suggested that the pulse-shaping techniques could achieve tenfold compression in aluminum-slab targets.[23]

Existing quasi-isentropic and multiple-shock capabilities are not now able to generate both very high compressions and low temperatures. Nevertheless, these methods appear to have long-range promise, and so we have extended the calculations in this paper beyond the current experimentally accessible range up to as high as tenfold compression. In fact, we find a nearly $V^{-2/3}$ energy-scaling relation of the Cu x-ray-absorption structure in the EXAFS region over this full range of volume, which may well offer a valuable volume diagnostic as these techniques develop.

In the remainder of this paper we report equation-of-state, electronic-structure, and x-ray-absorption calculations for Cu in Secs. II, III, and IV, respectively. A discussion of the results, and our conclusions, are presented in Sec. V.

II. EQUATION OF STATE

The theoretical techniques used in the present work directly provide the x-ray-absorption spectrum as a function of compression or volume. In order to also correlate these results with the applied pressure, an accurate pressure-volume relation of Cu is needed. Since neither experimental data nor rigorous calculation of this relation are available up to the compressions of interest here, we have carried out such calculations ourselves, and report them in this section. Furthermore the augmented-plane-wave (APW) method used for this purpose has also provided the self-consistent one-electron potentials used in the electronic-structure and x-ray-absorption calculations described in the remainder of the paper. To assess the accuracy of our APW $T=0$ pressure-volume relation, we have used a second electron-band-structure technique, the linear muffin-tin orbitals (LMTO) method, for comparison, and have also made a comparison with what limited experimental data is available. The results are given in Table I as a function of compression, V_0/V, where $V_0=79.70$ bohrs^3 is the experimental room-temperature zero-pressure volume per Cu atom.

The APW method[24] and the particular computer program used[25] have been described elsewhere. The calculations were nonrelativistic and employed the Hedin-Lundqvist exchange-correlation potential.[26] All electrons were treated self-consistently, and because of the extreme compressions considered, the $3s$, $3p$, and higher-lying states (19 electrons in all) were treated in a band mode. For compressions $V_0/V \geq 2$, all states were sampled with 20 points in the irreducible wedge of the fcc Brillouin zone. For lower compressions, the $3s$, and $3p$ levels were samples with 20 points per irreducible wedge, and the $4s$, $3d$, and higher-lying states with 89 points per wedge. In all cases, tests with reduced Brillouin-zone sampling indicated that the $T=0$ APW pressures P_0 in Table I are converged to better than 1%, or to within about 8 kbar for the first three entries in the table.

The LMTO method[27,28] and the computer program used[29] have also been described elsewhere. While the present LMTO calculations assumed the exchange-correlation potential of von Barth and Hedin,[30] tests for neighboring Ni have shown the calculated pressures to be negligibly different from those obtained using the Hedin-Lundqvist potential.[31] As in the APW calculations, all electrons were treated self-consistently, and the same Brillouin-zone—sampling choices were made for the same band electrons. Components through g character were included in the angular-momentum basis, as it was found that inclusion of g components reduced the pressure by 3% at the highest compressions considered. Both the

TABLE I. Calculated APW and LMTO $T=0$ pressures P_0 for Cu as a function of compression V_0/V. These P_0 results omit zero-point corrections and are nonrelativistic; relativistic pressure corrections are given by ΔP_{rel}. For comparison, room-temperature pressures P_{room} (reduced from shock data) as well as Hugoniot pressures P_H and temperatures T_H are shown. Pressures are in Mbar and temperatures in eV.

V_0/V	APW P_0	LMTO P_0	LMTO ΔP_{rel}	P_{room}[a]	P_H[b]	T_H[c]
1	−0.038	−0.078	−0.046	0.0	0.0	0.025
1.1	0.134	0.088	−0.054	0.164	0.168	0.032
1.2	0.372	0.323	−0.063	0.389	0.409	0.051
1.3	0.672	0.632	−0.072	0.685	0.746	0.100
1.4	1.064	1.012	−0.082	1.066	1.209	0.193
1.5	1.543	1.492	−0.092	1.548	1.843	0.327
2	5.456	5.450	−0.146			
3	22.67	22.92	−0.30			
5	105.2	106.0	−0.9			
7	257.5	260.2	−1.3			
10	617.9					

[a]Reference 40.
[b]Reference 42.
[c]Reference 43.

combined-correction term to the atomic-sphere approximation[27] and the muffin-tin[32] (or Ewald[33]) correction were included in these LMTO calculations. The muffin-tin correction significantly improves agreement between the LMTO and APW calculated pressures, which is not surprising, as it may be derived from the muffin-tin expressions[34] used in APW calculations in the limit in which the muffin-tin radius is extended to the Wigner-Seitz radius. The LMTO P_0 values in Table I already include this positive correction, which is 0.062, 0.272, and 2.1 Mbar for $V_0/V=1$, 2, and 5, respectively. They are also nonrelativistic for direct comparison to the APW results. Both omit zero-point corrections. Our LMTO program can also be run in a scalar-relativistic mode, in which only the spin-orbit relativistic effect is neglected. The resultant change in the LMTO pressure is given by the quantity $\Delta P_{\rm rel}$ in Table I.

A Murnaghan[35] fit to the first three APW pressures P_0 in Table I, plus a 9-kbar zero-point correction, yields a $T=0$ equilibrium lattice constant of 6.787 bohrs and a bulk modulus at the experimental equilibrium volume of 1.51 Mbar. These values are in close agreement with similar Korringa-Kohn-Rostoker (KKR) calculations of these quantities,[36] and in good agreement with experiment[37] (6.809 bohrs and 1.42 Mbar, respectively). The agreement with experiment is partly fortuitous in light of the nontrivial relativistic corrections in the fourth column of Table I, which improve the bulk modulus, but reduce the APW equilibrium lattice constant by 1%. The LMTO pressures plus relativistic corrections yield an equilibrium lattice constant smaller yet by about another percent, consistent with other LMTO calculations for transition metals.[38]

It is important to note that the percentage differences between LMTO and APW pressures in Table I, as well as the percentage of the relativistic correction, diminish with compression. Nevertheless, we expect our relativistically corrected (i.e., $P_0+\Delta P_{\rm rel}$) APW results to be the most rigorous in Table I. An interesting comparison is provided by the room-temperature pressures (fifth column in Table I) used in calibration of the ruby-fluorescence scale,[39] which were obtained by theoretical reduction of shock data.[40] As the total 293-K nuclear vibrational contribution to the pressure is about 0.022—0.030 Mbar for pressures ranging from 0 to 1 Mbar,[41] our relativistically corrected $T=0$ APW pressures are in excellent accord with the volume dependence of this room-temperature isotherm, but too low by about 0.06 Mbar. We do not know the cause of this discrepancy.

The last two columns in Table I give the experimental pressures[42] and calculated temperatures[43] along the Hugoniot or shock-compression curve for Cu. It has been predicted[43] that Cu will melt along the Hugoniot curve at a temperature of 0.45 eV, at $V_0/V=1.54$. This compression is well within the region accessible by both mechanical and laser-driven shock-compression techniques, and beyond the current $V_0/V\lesssim 1.3$ limitation of the diamond anvil for this material. Our $T=0$ x-ray-absorption calculations should apply throughout much of the solid phase, as the electrons are still highly Fermi degenerate, and the shape of the leading edge is mostly determined by the core-state lifetimes. The existence of Fermi degeneracy may be checked by comparing the Hugoniot temperatures in Table I to the width of that part of the $4s,3d$ valence band lying below the Fermi energy. This width in eV is approximately $\exp[2.2(V_0/V)^{1/3}]$ for $V_0/V<5$. As temperature is increased, thermal disorder of the lattice will eventually broaden the x-ray-absorption features beyond that due to lifetime effects. Nevertheless, if this broadening is symmetric and does not obscure the dominant features, the volume dependence of the present x-ray-absorption calculations may apply to shock-compressed Cu for V_0/V approaching 1.5.

Our calculations are clearly directly applicable to room-temperature diamond-anvil compression for both volume and pressure dependence. As we have discussed earlier, the full volume range of our calculations is also relevant to quasi-isentropic compression, either by multiple weak shocks, or by impactors with density gradients,[21] which could achieve relatively cold compressions well beyond $V_0/V=1.5$ in the solid phase.

III. ELECTRONIC STRUCTURE

An essential constituent of the x-ray-absorption calculations to be described in the next section is the electronic structure of the material under consideration. In this section we report calculations of the one-electron energy bands and density of states over a broad range of energy for fcc Cu as a function of compression. While the x-ray-absorption calculations require the angular-momentum-decomposed density of states, at this point we focus on the total density of states in order to more simply illustrate systematic trends in the evolution of the electronic structure in Cu with compression.

Especially at high energies, where the electron bands are quite steep, a fine sampling of the Brillouin zone is necessary to accurately model the density of states, and a band-structure technique that is considerably faster than the APW method used in the preceding section is required. The broad energy range considered also requires simultaneous treatment of more than one principal quantum number for a given value of the angular momentum, which is not easily accomplished with either the standard LMTO or linear—augmented-plane-wave (LAPW) methods.[27] The band-structure calculations reported in this section, therefore, have used a recent modification[11,12] of Andersen's LAPW method,[27] designed to fulfill both requirements. Calculations were carried out including all relativistic contributions except for spin-orbit (scalar-relativistic) contributions, up to dimensionless energies[44] of $ES^2\sim 100$ (about 190 eV for $V_0/V=1$), where S is the Wigner-Seitz radius ($4\pi S^3/3=V$, the volume per atom). At each compression V_0/V, this energy range has been divided into three panels for separate computation, chosen to maximize the accuracy of the calculated projected density of states over the entire range of interest. For the lowest panel, at both $V_0/V=1$ and 2 we have retained angular-momentum components through $l=4(g)$, while for all other panels and all other compressions angular-momentum components through $l=8$ have been retained. In all cases, the Brillouin zone has been sampled with 256

$\vec{k}$ points in the irreducible wedge for the fcc structure.

The current version of our LAPW program is not self-consistent. Since our APW calculations for the equation of state already provide suitable self-consistent muffin-tin potentials, we have used these in the LAPW calculations. It should be noted, however, that we perform scalar-relativistic LAPW x-ray-absorption calculations using these nonrelativistic APW potentials. While this procedure incurs errors of about 20 eV in the position of the $1s$ level (out of $\sim$9000 eV), and thus in the location of the absorption edge, our primary interest in this work is in the location of structure relative to the absorption edge. In this regard there is no problem, as we have demonstrated by the following LMTO calculations: We have performed scalar-relativistic calculations of the logarithmic derivative $D_l(E)$ of the radial component of the one-electron wave function, both for self-consistent nonrelativistic and scalar-relativistic potentials. The difference in the inverse of these functions $E_l(D)$ for fixed D in the two cases is a measure of the error in the band structure incurred by our procedure. We find these shifts at $V_0/V=1$ to be less than 0.34 eV, for $l=0$–5, and for energies ranging up to nearly 300 eV above the Fermi level. At higher compressions the shifts are also similarly quite small in relation to both the structure and scale of the x-ray-absorption features reported in this work.

The effects of pressure on the overall electronic structure of Cu are shown in Fig. 1, where we plot the Wigner-Seitz band-edge positions as a function of compression. The energies are relative to the muffin-tin zero of energy v_{MT} and the energy axis is in the dimensionless units[44] of ES^2. Cu has eleven electrons in the

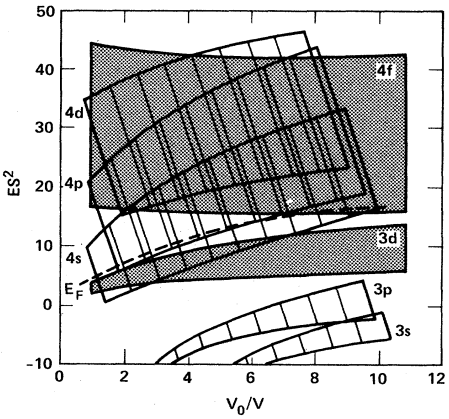

FIG. 1. Relative band positions for fcc copper as a function of compression V_0/V determined from the Wigner-Seitz band-edge positions. The energies (in Ry) are relative to the muffin-tin zero of energy at each compression, and are presented in the scaled dimensionless units ES^2, where S is the Wigner-Seitz radius (in bohrs).

$4s$-$4p$-$3d$ valence band, and aside from the effects of hybridization, which are neglected in Fig. 1, the $3d$ band remains completely filled throughout the entire range, $V_0/V=1$–10, shown in the figure, as is evident from placement of the Fermi level E_F. In fact, both the $3d$ and $4f$ bands drop in energy under compression, relative to the lower angular-momentum bands (although, of course, all the bands move up under pressure relative to E_F). This reflects the low kinetic energy of the nodeless $3d$ and $4f$ radial wave functions, compared to other states, and the

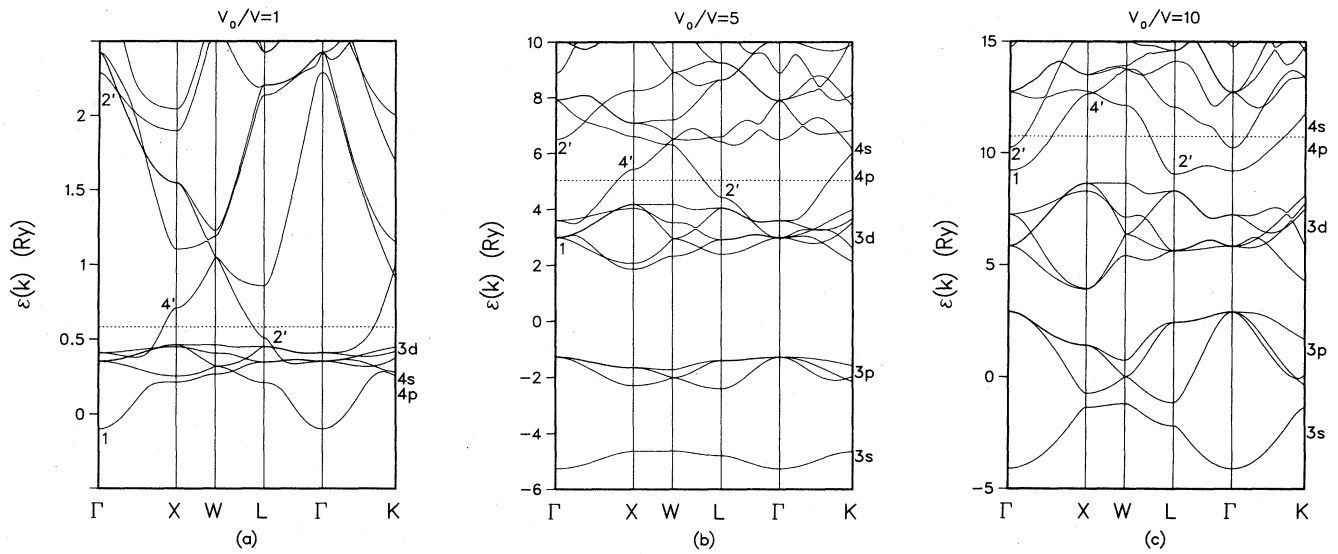

FIG. 2. Fully hybridized scalar-relativistic energy bands of fcc copper along symmetry directions. These bands were generated by the same LAPW code used to calculate the x-ray-absorption spectra. These plots were made by ordering the energy bands at each $\vec{k}$ point and connecting the different band points with straight-line segments band by band in increasing order of energy. The lines are thus a guide to the eye in the sense that no attempt was made to draw the lines to match bands of the same or related symmetry across points where the energy bands cross. (a), (b), and (c) show the bands at normal-density ($V_0/V=1$), at fivefold, and at tenfold compression, respectively. To aid the discussion in Sec. III, some symmetry labels have been added. On the right-hand side of the plots we have also added the labels $3s$, $3p$, $3d$, $4s$, and $4p$ (where appropriate) to indicate roughly the atomic origin of the bands.

growing importance of kinetic versus potential energy as volume decreases due to the different scaling, $V^{-2/3}$ and $V^{-1/3}$, respectively, of these contributions. Ultimately, the $3d$ band drops entirely below the $4s$ band, as seen near $V_0/V \sim 7$. The same phenomenon occurs for nickel, which, with one less valence electron, is predicted to have a region of insulating behavior at very high compressions.[31] The additional electron in Cu occupies the bottom of the $4s$ band at this point, and is predominantly s in character, although with increasing f content, as further compression brings the initially unoccupied $4f$ band closer to and then below the Fermi level.

This evolution is more precisely shown in Figs. 2(a), 2(b), and 2(c), where we give the fully hybridized scalar-relativistic energy bands along symmetry directions for $V_0/V=1$, 5, and 10, respectively. For $V_0/V=1$ [Fig. 2(a)] the $4s$ band extends from Γ_1 to the mostly p-like X_4' level, and is crossed by and hybridized with the narrow $3d$ band near $E=0.4$ Ry. At $V_0/V=5$ [Fig. 2(b)], the bottom of the $4s$ band Γ_1 lies in the middle of the $3d$ bands, while by the time $V_0/V=10$, it has moved above the $3d$ bands. The L_2' state, which lies just above the $3d$ bands and just below E_F, is initially of pure p character. Under pressure it becomes increasingly f-like and, by the time $V_0/V=10$, it represents the bottom of the $4f$ band, which then lies below E_F. One can also see the downward movement of the $4f$ band by observing the drop of Γ_2', which is a pure $4f$ state. From Fig. 2 it is evident that this trend will continue for $V_0/V \geq 10$, where we would expect Γ_1 to rise above Γ_2', and for Γ_2' to merge into the $3d$ band with a resulting $3d$-$4f$ conduction band near the Fermi energy.

Under compression the $3s$ and $3p$ core states broaden and must be treated as bands for $V_0/V \geq 3$. They are the bottom two bands shown in Figs. 2(b) and 2(c). One should also observe that the $3s$ and $3p$ core states have nearly merged together by the time $V_0/V=10$, and that the gap separating them from the $3d$ band is beginning to close. At higher compression the $3s$, $3p$, $3d$, and $4f$ (and higher-lying) bands will all merge into one continuous conduction band.

Figures 3(a), 3(b), and 3(c) give the total density of states $D(E)$ for Cu at $V_0/V=1$, 5, and 10, respectively, corresponding to the band structure plotted in Fig. 2. In each case, $D(E)$ is shown only above the muffin-tin zero, which is taken to be the zero of energy in these figures. The smooth dashed lines are the familiar free-electron density of states $(V/2\pi^2)E^{1/2}$, shown for comparison, which give a reasonably good average of the band-structure $D(E)$ at high energies. This is consistent with the expectation of increasing free-electron-like behavior at high energies as the large electron kinetic energy begins to dominate the relatively weaker Coulombic interactions. One also expects increased free-electron-like behavior at high compressions, due to the different scaling of kinetic and potential energies mentioned above, although this is not particularly evident in Fig. 3. Both limits may be better understood with the help of a simple model calculation based on the Friedel sum rule.[45]

For a single muffin-tin potential embedded in the electron gas, the number of states $N(E)$ below energy E is

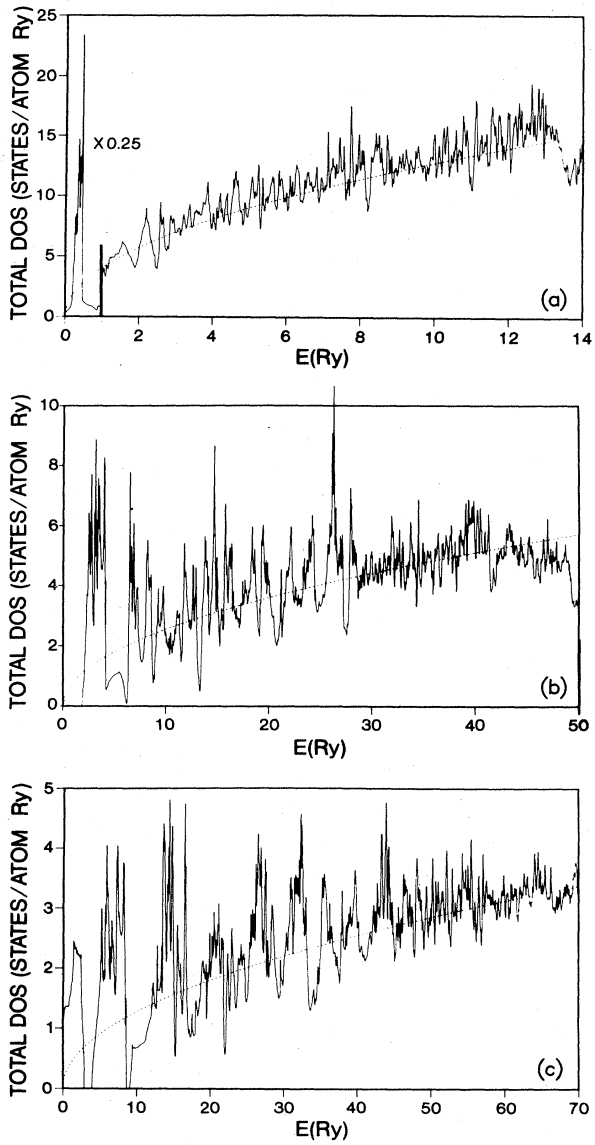

FIG. 3. Total density of states (including both spins) of compressed fcc copper. The jagged solid line was calculated from the same LAPW code that was used to calculate the x-ray-absorption spectra. The smooth dashed line, the simple free-electron parabolic density of states, is shown for comparison. (a), (b), and (c) are the results for normal-density, fivefold, and tenfold compression, respectively. The energy scales along the x axis of each part of the figure are relative to the respective muffin-tin zero at each compression. In (a) the normal-density $3d$ band (between 0 and 1 Ry on the plot) has been multiplied by a factor of 0.25 to keep it within the scale of the figure.

given by

$$N(E)=\frac{V}{3\pi^2}E^{3/2}+\sum_l 2(2l+1)\frac{\delta_l(E)}{\pi}\ , \tag{1}$$

and the density of states by $D(E)=dN(E)/dE$. The first term corresponds to the unperturbed electron gas, while the second (Friedel sum) gives the additional number of states arising from the "impurity" muffin-tin potential.

One may view Eq. (1) as the first two terms in an expansion of the crystal $D(E)$, with successive terms introducing the effects of multiple scattering of the electrons by the full lattice of muffin-tin potentials comprising the crystal.[46] Yet it is interesting to note that the two terms of Eq. (1) alone yield the correct number of electrons in Cu to within 0.5 electrons, over the entire compression range considered in this paper, when it is evaluated at the APW (or LAPW) Fermi energy E_F, with phase shifts $\delta_l(E)$ obtained from the APW potentials. Since the first term in Eq. (1), evaluated at E_F, varies from about one to nine electrons throughout this compression range, this agreement is not accidental, and lends credence to our use of Eq. (1) to interpret Figs. 3(a)—3(c).

Figure 4 shows the second term of Eq. (1), the Friedel sum (solid curves) evaluated using phase shifts $\delta_l(E)$ obtained from the APW potentials at various compressions, as a function of the dimensionless energy ES^2. The phase shifts were chosen so that $\delta_l(\infty)=0$, and thus according to Levinson's theorem[47] the Friedel sum gives the number of bound states in the muffin-tin potentials as $E\rightarrow 0$ (which we take to be the muffin-tin zero). As can be seen, there are 18 bound states for all the highest compression, $V_0/V=10$, where the $3p$ level has moved into the continuum as a resonance. The sharp rise in the solid curves near the middle of the figure is, of course, the $3d$ resonance, and the Fermi level lies, in each case, somewhat above this resonance in energy. Away from the $3d$ resonance, the Friedel sum for $V_0/V=1$ is seen to be quite flat up to energies well above the Fermi energy ($E_F S^2=4.1$). In this flat region, $D(E)$, which is the energy derivative of $N(E)$, will be dominated by the free-electron $(V/2\pi^2)E^{1/2}$ term, and it can be seen why the electronic structure of normal-density Cu is considered to be very-free-electron-like, except near the $3d$ band.

The evolution towards free-electron behavior both at high energies and at high compressions can also be clearly seen in Fig. 4, and arises from rather different behavior of the Friedel sum. At high energies, where high-l δ_l are increasingly important, elementary scattering theory[48] shows the Friedel sum to approach the limiting behavior of $(V/2\pi^2)E_0E^{1/2}$, where the volume-dependent E_0 is given by

$$E_0=\frac{4\pi}{V}\int_0^{R_{\mathrm{MT}}} r^2 v(r)dr\ , \tag{2}$$

and where R_{MT} and $v(r)$ are the muffin-tin radius and potential, respectively. In this limit Eq. (1) becomes the first two terms in a Taylor expansion of $(V/3\pi^2)(E-E_0)^{3/2}$, the continuum-lowered free-electron $N(E)$. When plotted against ES^2, the limiting form of the Friedel sum is only weakly dependent on compression, and is shown as the shaded region in Fig. 4. Thus the upward bend in the solid curves to the right in Fig. 4 shows the approach to free-electron behavior at high energies, while the overall downward shift of these curves with compression shows the approach towards the free-electron behavior (shaded region) at high compression. In the limit of extremely large compressions, far beyond the $V_0/V=10$ limit considered here, all bound states of the muffin-tin potential will have moved into the continuum,

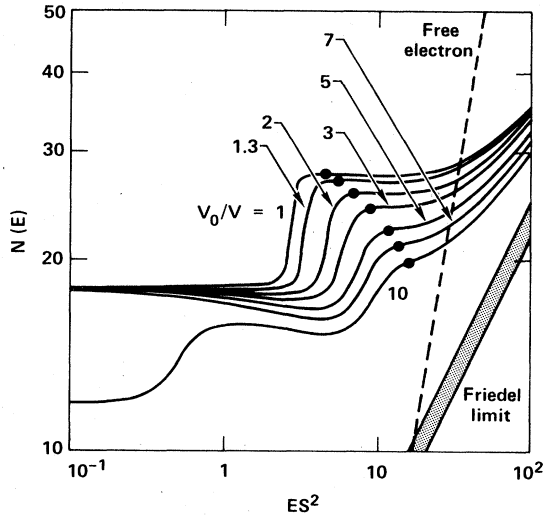

FIG. 4. Friedel-sum contribution (solid line) to the number of states per atom $N(E)$, as a function of scaled energy ES^2, where S is the Wigner-Seitz radius, for compressions $V_0/V=1$, 1.3, 2, 3, 5, 7, and 10. For comparison, we have also shown the high-energy limit, $(V/2\pi^2)E_0E^{1/2}$, of the Friedel sum (shaded region) and the free-electron result (dashed line). The large dots on each of the solid lines indicates the position of the Fermi energy for each compression.

with sufficiently large resonance widths, so that the initial "staircase" structure of the Friedel sum will have evolved into smooth $E^{1/2}$ behavior at all energies.

The dashed curve in Fig. 4 shows the first term in Eq. (1), which is much larger than the Friedel-sum contribution for energies above $ES^2\gtrsim 30$. Because of its much larger slope than the Friedel sum (away from the $3d$ resonance), the derivative of the first term also dominates the Friedel contribution and explains the good average agreement of $(V/2\pi^2)E^{1/2}$ (the smooth solid curves) with the band-structure $D(E)$ in Figs. 3(a)—3(c) over much of the upper range of energy plotted.

In Table II we present results for the Fermi energy and the density of states at the Fermi energy. For the band-structure LAPW results, the Fermi energy E_F moves up relative to the muffin-tin zero of energy v_{MT} as the system is compressed. This increase reflects both the increase of kinetic energy of the electron states under compression, as well as the broadening of the conduction band. The density of states, evaluated at the band-structure E_F, decreases under compression, and hence is consistent with the increasing bandwidths with increasing pressure. The free-electron results shown in Table II for comparison correspond to the first term of Eq. (1) and its energy derivative. The Fermi energy was determined by filling these states with one electron per atom. The density of states evaluated at the free-electron value of E_F agrees surprisingly well with the band-structure density of states. Nonetheless, since the free-electron F_F values are so much lower than the band-structure values, and since there is so much structure in the band-structure $D(E)$ near E_F, we believe the agreement is probably fortuitous.

Finally, we observe that the fine-scale structure in the

TABLE II. Fermi energy E_F (in Ry) and the density of states at the Fermi energy $D(E_F)$ (in states/atom Ry) as a function of compression V_0/V. The band-structure results are given first, and for comparison purposes the free-electron-model results, corresponding to the first term in Eq. (1), are also presented. To aid in interpreting the figures, the Wigner-Seitz radius S (in bohrs) and the scaled band-structure Fermi energy S^2E_F are also shown.

			Band structure		Free electron	
V_0/V	S	S^2E_F	E_F	$D(E_F)$	E_F	$D(E_F)$
1	2.670	4.15	0.58	4.0	0.52	2.9
1.3	2.446	5.10	0.85	3.4	0.62	2.4
2	2.119	6.93	1.54	2.4	0.82	1.8
3	1.851	8.99	2.62	1.6	1.08	1.4
5	1.561	12.26	5.03	1.0	1.51	1.0
7	1.396	14.57	7.48	0.85	1.89	0.79
10	1.239	16.50	10.75	0.74	2.40	0.63

band-structure density of states, Figs. 3(a)—3(c), seems to increase in amplitude with compression. This increase is real and is a consequence of a stronger scattering amplitude from the compressed copper potentials. Although the density of states as a whole in Cu may be approaching increased free-electron-like character as $V_0/V\rightarrow 10$, individual phase shifts may move through regions of strong scattering [$\delta_l\sim(\frac{1}{2}+\text{integer})\pi$] in their continuing decrease with compression towards the ultimate free-electron limit. Indeed, a calculation of the backscattering amplitude shows this to be happening for Cu as $V_0/V\rightarrow 10$. We will elaborate on this point more fully in Sec. IV when we discuss the magnitude of the structure in the x-ray-absorption spectra.

IV. X-RAY-ABSORPTION SPECTRA

The simplest and most direct probe of the unoccupied electronic states is the x-ray-absorption spectrum. The K and L_1 edges, which arise from $1s$ and $2s$ core excitation, respectively, probe the p component of the unoccupied density of states, while the $L_{2,3}$ edges, which arise from the $2p$ core excitation, mainly probe the d component, since the s component, which is also allowed by selection rules, is usually strongly suppressed by matrix elements.

More specifically, the x-ray-absorption spectra from a core state Ψ_c with quantum numbers $c=nlj$ ($j=l\pm\frac{1}{2}$) and energy E_c due to a photon of energy $\hbar\omega$ is given by[49]

$$\mu_c(\hbar\omega)=\frac{4\pi e^2}{3\hbar cV}\frac{2j+1}{2(2l+1)}(\hbar\omega)^2 \times\left[\frac{l}{2l+1}f_{c,l-1}(\hbar\omega+E_c)+\frac{l+1}{2l+3}f_{c,l+1}(\hbar\omega+E_c)\right], \quad (3)$$

where the partial strength $f_{c,l}(E)$ can be factorized into

$$f_{c,l}(E)=r_{c,l}^2(E)D_l(E)\ . \quad (4)$$

Here, $D_l(E)$ is the partial density of states defined by

$$D_l(E)=2\sum_{\vec{k},n}\delta(E-E_{\vec{k}n})\sum_m|\langle lm\,|\,\Psi_{\vec{k}n}\rangle|^2\ , \quad (5)$$

where we have labeled the energy-band states with the reduced wave vector $\vec{k}$ and the band index n. The effective dipole matrix element $r_{c,l}(E)$ is given by

$$r_{c,l}(E)=\frac{\langle\Psi_c r\phi_l(E)\rangle}{\langle\phi_l^2(E)\rangle^{1/2}}\ , \quad (6)$$

where the partial wave $\phi_l(E)$ is a solution of the radial Schrödinger equation with energy E for a single muffin-tin sphere, and the angular brackets in Eq. (6) denote a radial integral. The integrations in Eq. (6) extend over the Wigner-Seitz sphere. The error introduced in replacing the primitive cell by a sphere of the same volume in these integrals is negligible.

The calculated μ_c for each edge will be referred to as the raw spectra, and, by energy conservation as well as the Fermi exclusion principle, is zero if $\hbar\omega<E_F-E_c$. These spectra have been computed assuming sharp core and band energies. For comparison with the absorption coefficient that would be seen experimentally, we have also calculated the broadened spectra, $\bar{\mu}_c(\hbar\omega)$, as

$$\bar{\mu}_c(\hbar\omega)=\frac{1}{2\pi}\int_{E_F}\frac{\mu_c(E)\Gamma(E)}{(\hbar\omega-E)^2+\Gamma^2(E)/4}dE\ , \quad (7)$$

where the lower limit of the integral, the Fermi energy E_F, is the edge threshold. More precisely, we use Eq. (7) twice to obtain the broadened spectra. The first time, we use an energy-independent Lorentzian broadening function Γ_c to take into account the core-hole width. We then use Eq. (7) again on the resulting spectra, this time with an energy-dependent $\Gamma_x(E)$, where $\Gamma_x(E)$ is the width of the excited band-energy state. Note that we have not in-

TABLE III. Core-hole widths Γ_c used in the broadened spectra for the K and L edges.

	Width	
Core hole	(eV)	(Ry)
Γ_K	1.5	0.11
Γ_{L_1}	9.2	0.68
Γ_{L_2}	1.4	0.10
Γ_{L_3}	1.0	0.07

cluded any broadening due to experimental resolution nor any many-body effects such as the influence of the core hole on the band states.

Since the pressure dependence of the core-hole and excited-state widths is not accurately known, we have used our best normal-density values for all compressions. The core-hole lifetimes that we used[50–55] are given in Table III. For the excited-state widths, $\Gamma_x(E)$, we have taken our best estimate of the mean free path $\lambda_x(E)$, of Refs. 56 and 57, and used the formula[58]

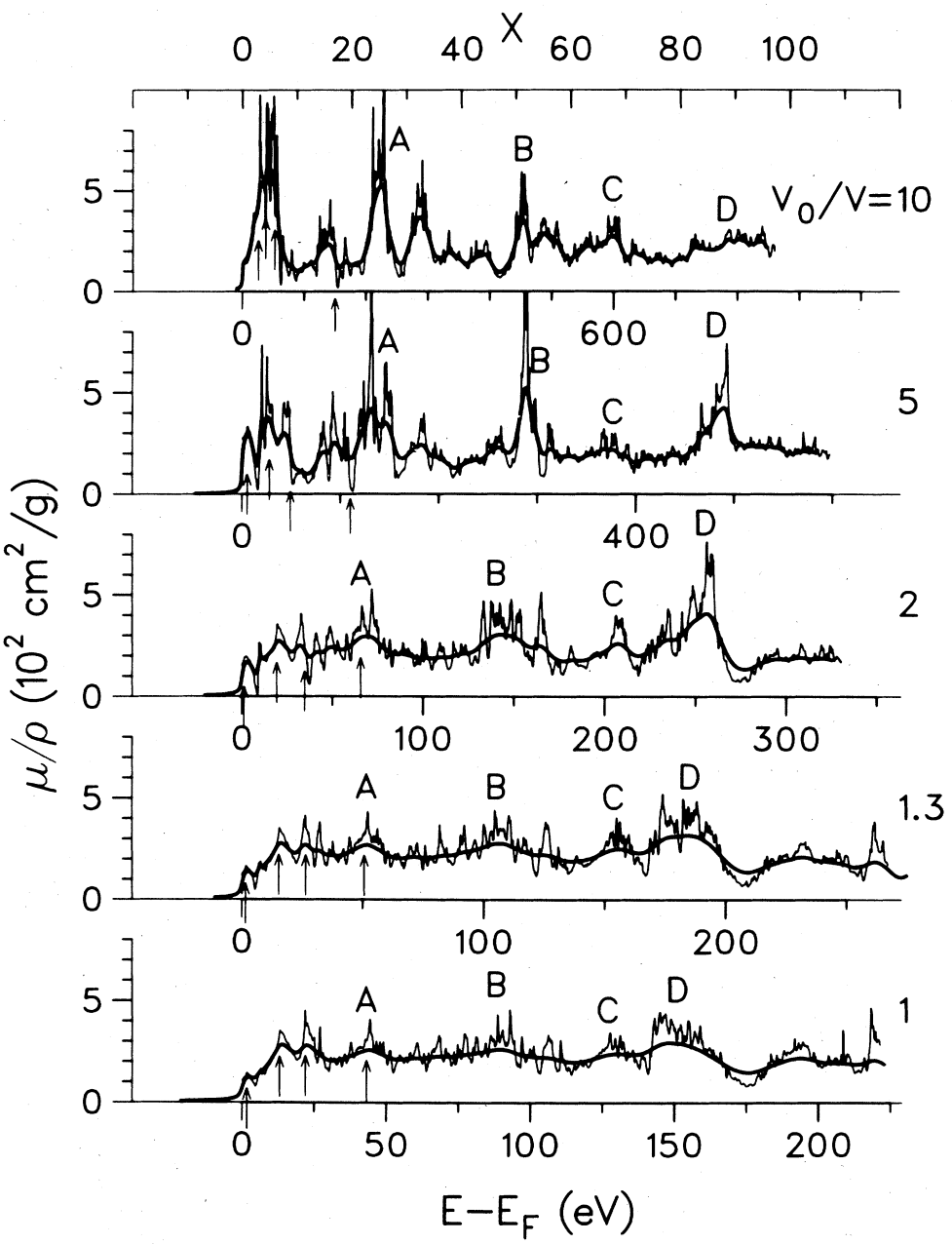

FIG. 5. K-edge x-ray-absorption coefficients μ/ρ for fcc copper as a function of compression V_0/V. Two curves are superimposed at each compression (which is indicated on the right-hand edge of each plot). The heavy solid curve is the final-state and core-hole broadened spectra. The lighter solid line is the unbroadened spectra. The energy axes are in units of eV for each compression. The zero of energy is E_F with respect to the energy of the outgoing final-state electron or the K-edge position with respect to the spectra. With respect to each other, the energy scales for the different compressions are scaled as $x=(E-E_F)S^2$. For clarity, we have added this additional scale at the top of the figure, which, of course, applies to all the plots below it (i.e., for all compressions). The four arrows, from left to right (in order of increasing energy), at each compression indicate the energies of an X_4', X_5', and L_3', and another L_3' electron-energy-band point. For the compressions $V_0/V=5$ and 10, some of the highest peaks in the unbroadened spectra have been truncated to keep the curves within the plots.

$$\Gamma_x(E)=\frac{\hbar}{\tau_x}=\frac{\hbar v_x}{\lambda_x}=\frac{\hbar[2(E-E_F)/m]^{1/2}}{\lambda_x} . \quad (8)$$

A plot of $\Gamma_x(E)$ is given in Fig. 1 of Ref. 10. In Sec. V we discuss our neglect of the pressure dependence of the broadening.

In Figs. 5—8 we show the K- and L-edge x-ray-absorption calculations as a function of compression. Because of uncertainties about the correct broadening under pressure, we show both broadened and unbroadened spectra superimposed on the same plot. Except for an overall factor of 2, the L_2 and L_3 edges are virtually identical and we therefore only show the L_2 edge. Since the spin-orbit splitting that separates the energy positions of these two edges is small, we have superimposed these two spectra in Fig. 8 at the normal-density energy separation to suggest what the observable spectrum would roughly look like. Although this splitting will probably not change much under pressure (cf. Table IV and the discussion in the following section), if good calculations of the edge positions as a function of pressure should become available in the future, Fig. 7 could be scaled and superimposed on itself to provide a more realistic L_2-L_3—edge spectrum. We have not shown any M-edge spectra since the relevant core states ($3s$ and $3p$) broaden into bands at high pressure [cf. Figs. 3(b) and 3(c)].

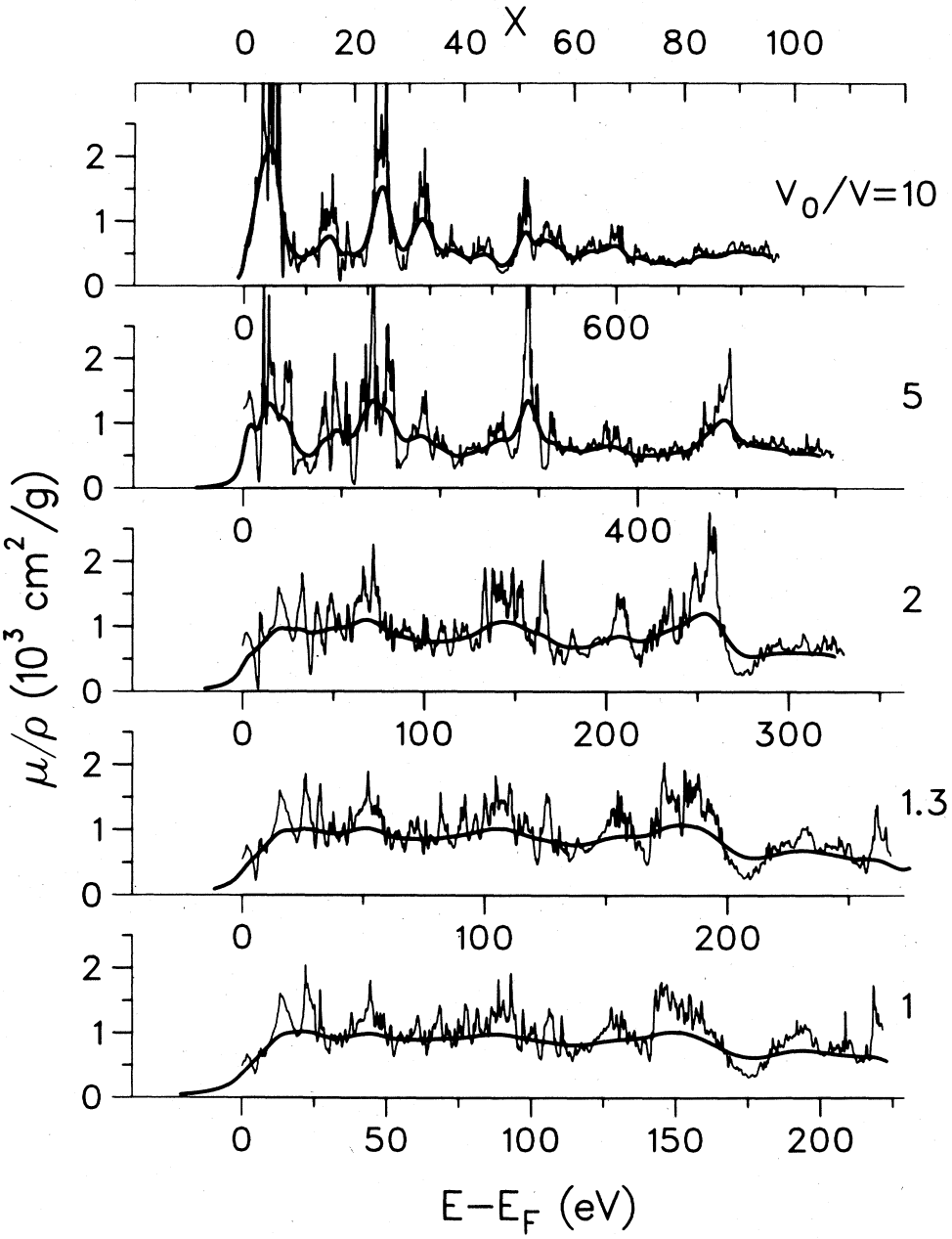

FIG. 6. L_1 edges of compressed fcc copper. The notation for this figure is described in the caption of Fig. 5. For the compressions $V_0/V=5$ and 10, some of the highest peaks in the unbroadened spectra have been truncated to keep the curves within the plots.

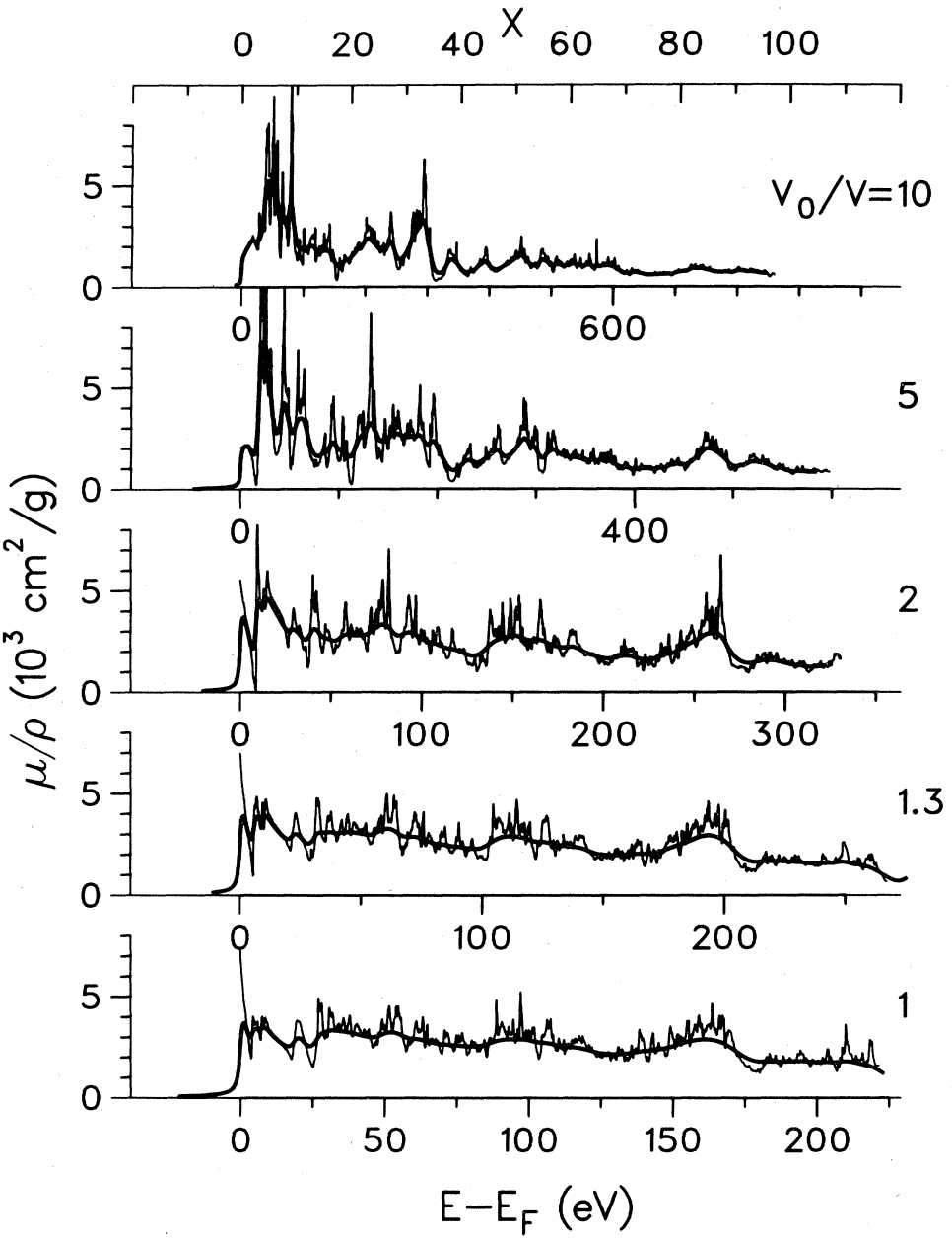

FIG. 7. L_2 edges of compressed fcc copper. The notation for this figure is described in the caption of Fig. 5. For the compressions $V_0/V=5$ and 10, some of the highest peaks in the unbroadened spectra have been truncated to keep the curves within the plots.

Instead of directly presenting our results for μ in the standard units of cm^{-1}, we instead show μ/ρ in units of cm^2/g. This scaling, by the mass density ρ, makes it easier to compare calculations for different compressions since it makes the results look more like an absorption per atom. Without the scaling, the absorption increases dramatically with compression because the incoming x-ray beam encounters more atoms to absorb it.

In Table V we demonstrate that the overall magnitude of the absorption[59] is roughly independent of compression. The values tabulated were obtained by an rms fit of the unbroadened $\mu(E)$ to $\ln\mu=\alpha+\beta\ln E$ over the range of energies shown in the figures, and then by extrapolating the fit back to the edge position. At normal density, experiment[16,60] gives $\mu_K/\rho=274.5$ cm^2/g after the background is subtracted out, as compared with 248.3 cm^2/g from the calculations. Thus the band-structure results at $V_0/V=1$ are about 9% too low and give an overall magnitude in good agreement with atomic calculations.[16,60] More elaborate atomic calculations suggest that this discrepancy is largely due to the neglect of core relaxation on the final-state wave functions.[61] Among other things, this means that the initial- and final-state wave functions are no longer orthogonal to each other since they experi-

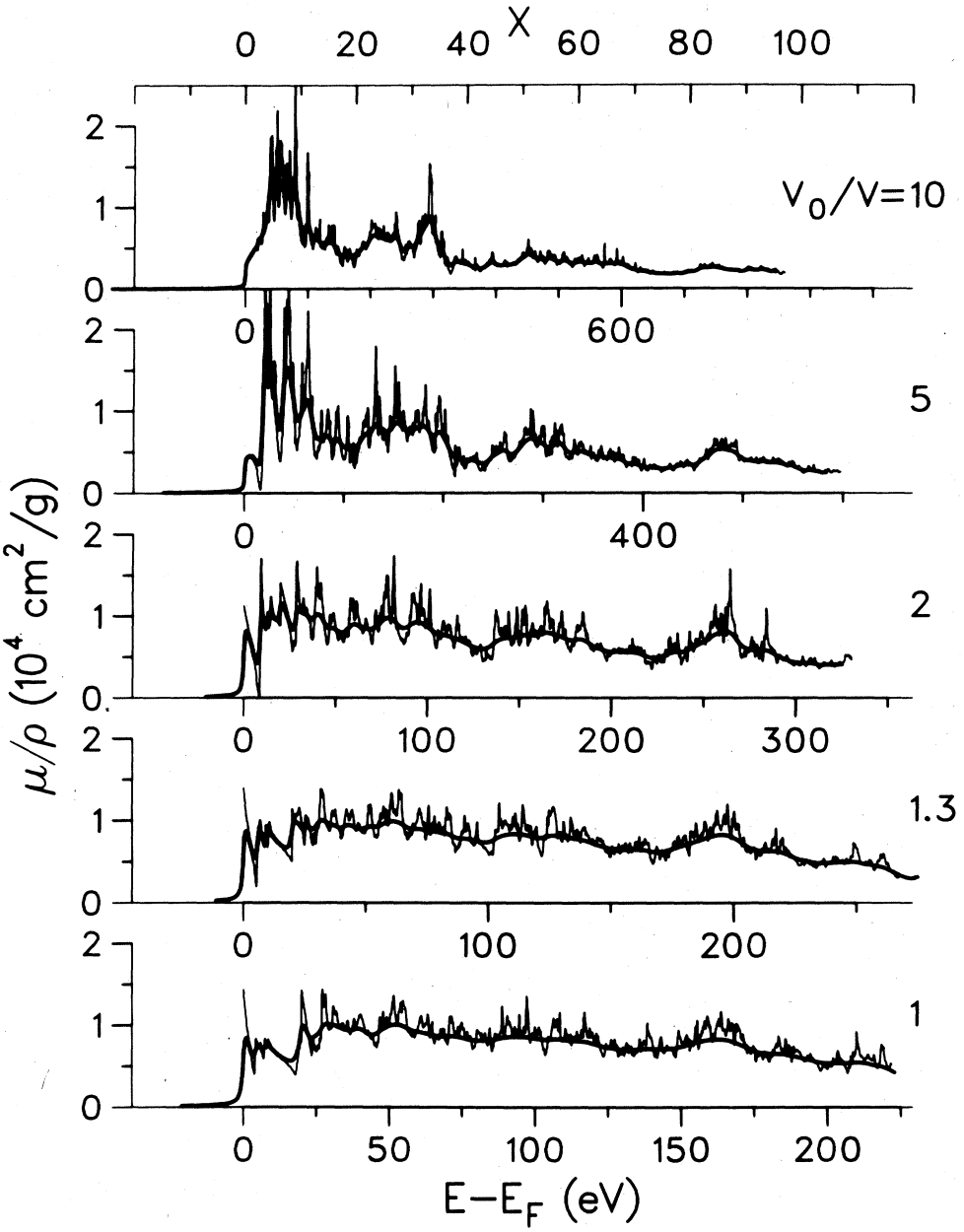

FIG. 8. L_2-L_3 edges of compressed fcc copper. The relative edge positions of the superimposed L_2 and L_3 edges for all compressions are assumed to have the same normal-density energy separations in all of these plots. Otherwise, the notation for this figure is described in the caption of Fig. 5. For the compressions $V_0/V=5$ and 10, some of the highest peaks in the unbroadened spectra have been truncated to keep the curves within the plots.

ence different potentials, and hence the matrix elements between Slater determinants no longer reduce to a single integral over the initial core wave function and final-band-state wave function. In short, many-body effects must be taken into account to handle the problem of core relaxation.[62]

The insensitivity of the overall magnitude to compression is probably a consequence of the sum rule on oscillator strength.[63] The decrease in the density of states with pressure is compensated for by increased strength in the squared matrix elements [cf. Eq. (4)].

The energy axes in Figs. 5—8 are scaled by $(V/V_0)^{-2/3}$

TABLE IV. Single-particle edge positions E_F-E_c for the K and L edges of Cu as a function of compression V_0/V.

	E_F-E_c (Ry)			
V_0/V	K	L_1	L_2	L_3
1	650.565	78.135	68.633	67.119
1.3	650.600	78.187	68.685	67.171
2	650.687	78.305	68.801	67.287
3	650.845	78.500	68.991	67.478
5	651.359	79.088	69.566	68.054
7	652.011	79.809	70.270	68.761
10	652.876	80.755	71.192	69.688

TABLE V. Average extrapolated absorption coefficient just above the K edge of Cu as a function of compression. For comparison, the normal-density experimental (Expt.) value is shown in the last (extreme right-hand) column.

	V_0/V						Expt.
	1	2	3	5	7	10	1
μ_K^+/ρ (cm^2/g)	248.3	242.9	250.2	264.5	253.7	292.8	274.5

for each compression where V_0 is the normal-density volume. Previous calculations at normal density[9–12] on other materials have shown the usefulness of this technique for correlating structure in the x-ray absorption. This scaling, which attempts to remove the increased kinetic energy of the electronic energies under compression, is even more essential if one is to understand the structure of the current results, which extend to such high pressures and compressions. Its essential correctness is demonstrated by examining the energy bands. With the same numbers of bands (about 120 for Figs. 5–8) the energy range needed to span those bands scales roughly like $V^{-2/3}$.

As might be expected, those states far above the Fermi energy, with the most extended wave functions and largest kinetic energies, fit this scaling best. For states just above the Fermi energy,[64] the potential energy nearly compensates for the kinetic energy, and this scaling works less well.

For the x-ray-absorption results, this shows up in the way the structure lines up in Figs. 5–7 once one reaches 20–30 eV or more above the edge (at normal density). In the energy range just at the edge, the x-ray absorption is more sensitive to the details of the pressure dependence of the band structure and the peaks can be correlated with specific band states. In Fig. 5 we show four arrows that mark the positions of the energy eigenvalues of an X_4', X_5', L_3', and another L_3' band point. As shown in Fig. 5, the first three points correlate well with the first three peaks of the x-ray absorption for $V_0/V=1$, and then faithfully follow these peaks as they coalesce into one giant peak at $V_0/V=10$. The fourth arrow is an example of attempts to correlate features in the x-ray absorption at higher energies above the edge. At $V_0/V=1$, the higher L_3' point lines up almost exactly at the center of the fourth peak (exact alignments should not be expected since broadening can shift the apparent peak positions), but under compressions it drifts away from the peak. Its alignment with the fourth peak for $V_0/V=1$ was apparently fortuitous.

From Figs. 3(a)–3(c) we can see that the density of states is small near the Fermi energy and grows roughly like $E^{1/2}$ at higher energies. Thus a few key states might be expected to dominate the spectra near the edge. At higher energies, so many states contribute to the spectra that it is less likely that any one could dominate enough to be considered the "cause" of the peaks in the structure. Also, it is important to remember that the final-state broadening at high energies is large enough so that peaks at high energy can survive only if the oscillator strength for those transitions remains high over an energy range of the scale of that width ($\geq \frac{1}{2}$ Ry), and hence must be strong for many states. Thus some other interpretation (such as EXAFS arguments or multiple-scattering effects) other than the details of the band structure must be invoked to explain the structure of the x-ray absorption at energies above the near-edge region. Near the edge, as we have just shown, band states at symmetry points (where symmetry forces the bands to come in flat with a resulting high density of states) with a large component of the required orbital-angular-momentum character (e.g., p-like character for a K or L_1 edge) can be well correlated with the x-ray peaks.

Above the near-edge region, at least four peaks in the $V_0/V=1$ K-edge spectra can be observed. These peaks are labeled A–D in Fig. 5. Under compression, these peaks generally grow in magnitude. Furthermore, between these peaks much additional structure is seen at the large compressions. Part of the increased amount of structure in the K-edge spectra (the same effect is seen in all the edges) might be expected to occur because the electronic states are spread out over a larger energy region, whereas the broadening function remains fixed. Hence the broadening would wash out more features at normal density. We have checked this effect by broadening our original spectra with a volume-scaled energy-independent broadening function $\Gamma=(0.05\ \text{Ry})(V/V_0)^{-2/3}$, which should compensate for the energy scaling under pressure. The results indicated that the increase in structure with pressure is so large that broadening effects are relatively unimportant. In other words, the effect is real and is not an artifact of the broadening.

We believe that the increased structure is due to an increase in the scattering amplitude of the muffin-tin potentials and correlates with the increased amplitude in the fine structure of the density of states seen in Figs. 3(a)–3(c). To quantify this hypothesis, we observe that the standard EXAFS x-ray-absorption formula is given

$$\mu = A\hbar\omega N_0[lM_{l,l-1}^2\chi_{l-1}+(l+1)M_{l,l+1}^2\chi_{l+1}]\ , \qquad (9)$$

where

$$\chi_l = 1+(-1)^l\sum_j N_j \mathrm{Im}\left[\exp(2i\delta_l)\frac{\exp(2ikR_j)}{kR_j^2}f(\pi)\right]. \qquad (10)$$

N_j and R_j are the number of atoms in shell j and the distance of that shell from the central atom (where the x-ray absorption takes place), respectively. See Ref. 65 for a detailed description of the notation.

The interference of scattered wavelets, returning to the central atom after backscattering from atoms in each shell, with the outgoing wavelet from the central atom, gives rise to band-structure-like effects. Indeed, barring

other approximations in Eq. (9), if all possible multiple scattering off all the neighboring atoms were included, one should build up the exact band-structure result. Note that χ_l in Eq. (9) plays the same role as the projected l-dependent density of states in Eq. (3) and is responsible for the x-ray-absorption structure in Eq. (9), except for an overall very slow (in energy) modulation by the matrix elements. This modulation can greatly affect the magnitude of the absorption, but does not otherwise modify the structure much.

In Eq. (10), $k=E^{1/2}$, and hence we can rewrite it in the scaled form:

$$\chi_1=1+(-1)^l\sum N_j \mathrm{Im}\left[\exp(2i\delta_l)\frac{\exp[2i(ES^2)^{1/2}(R_j/S)]}{(ES^2)^{1/2}(R_j/S)^2}\left[\frac{f(\pi)}{S}\right]\right], \tag{11}$$

where S is the Wigner-Seitz radius. From this we can see that the magnitude of the interference scales in energy as ES^2, except possibly for the phase shifts, $\delta_l(E)$, and is proportional to the dimensionless quantity $f(\pi)/S$, where $f(\pi)$ is the standard 180° backscattering amplitude.

In Fig. 9 we show the absolute magnitude of the complex quantity $f(\pi)/S$ calculated from phase shifts of the APW potentials as a function of $x\equiv(E-E_F)S^2$ and compression. As a function of x, $f(\pi)/S$ shows a local maximum, which moves to smaller values of x as the compression increases. Because of this, $f(\pi)/S$ near $x\sim 20$ becomes more than 3 times larger at $V_0/V=10$ than at normal density, $V_0/V=1$. This same behavior is mirrored in the K-edge x-ray absorption, Fig. 5. Note that the peak labeled A ($x\sim 24$) in Fig. 5 grows considerably in amplitude as V_0/V increases from 1 to 10. Neighboring peaks show more or less the same behavior, until by the time peak D is reached ($x\sim 85$) the maximum amplitude is seen to occur more in the range $V_0/V=2$–3 than at higher compressions. However, this again is precisely what is indicated by $f(\pi)/S$ in Fig. 9 near this value of x. Furthermore, not only do the peak amplitudes in Fig. 5 correspond to variations in $f(\pi)/S$, but so too does the amount of structure in the x-ray absorption. More structure is seen to develop between peaks A and B as V_0/V increases, for example, which again corresponds with the increase in $f(\pi)/S$ in this region.

We have programmed a slightly generalized[65] version of the EXAFS equation (10) and compared the results with the full band-structure calculations of the x-ray-absorption edges, Figs. 5–8. The EXAFS calculations also have the same magnitude dependence of peaks as a function of energy and compression as the band-structure calculations, which suggests the intuitively plausible result that, as a rough first approximation, the magnitude or strength of the atomic scattering amplitude determines the size of the x-ray-absorption structure as a function of both energy and compression.

Moreover, the agreement between the EXAFS and band-structure results become increasingly worse whenever the backscattering amplitude becomes increasingly stronger. We believe that this is due to the shadowing of the fourth shell by the first shell of neighbors, an effect which is not included in the standard EXAFS formulations. We[66] are currently trying to add in these corrections to the more standard EXAFS results to see if they can restore agreement with the band-structure results for the case of strong scattering.

V. DISCUSSION

The method described in Sec. IV has been successfully used to explain experimental x-ray-absorption data.[9–13] In this section we point out some of the more poorly understood aspects of the underlying physics, which may slightly change the results in an unknown way with pressure, and discuss the implications of our calculations for developing a high-pressure density diagnostic.

The first concern is the core-hole binding energy. In the single-particle picture, the x-ray-absorption edge will begin at a photon energy of E_F-E_c (if we ignore broadening effects), where E_F is the Fermi energy and E_c is the core-state energy. For both solids and atoms, the experimental binding energy almost always differs from that predicted by the single-particle picture.[67–71] A large part of this difference is due to the relaxation of the surrounding electrons as the photoejected electron leaves the excited atom, which has absorbed the incoming photon. We will refer to this effect as core-hole relaxation. In principle, this effect could also change the structure of the x-ray-absorption edge, due to the ensuing many-body effects.[62] In practice, the successful application of the method described in Sec. IV seems to indicate that one

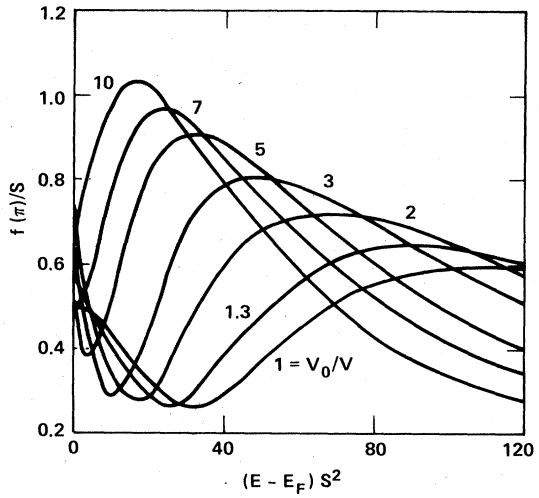

FIG. 9. Scaled backscattering amplitude $f(\pi)/S$ as a function of the scaled energy $(E-E_F)S^2$. Since $f(\pi)$ is a complex number with real and imaginary parts, we actually show only the absolute magnitude of $f(\pi)/S$ in order to simplify the plots.

can ignore changes in the structure of the x-ray-absorption edge due to core-hole relaxation for metals, possibly because of the extended nature of the final-state wave functions.

According to current theory,[72–76] the correct way to calculate the x-ray-absorption spectra is to use final-state wave functions for the excited electron, which are calculated in the presence of the relaxed core hole. This is difficult because it requires impuritylike calculations, where, since the central excited atom differs from the surrounding atoms, the simplicity of periodic boundary conditions is lost. In our calculations, we instead use the band-structure Bloch states for the final state of the outgoing electron and treat the effects of core-hole relaxation solely by shifting the x-ray edge to the experimentally observed edge at normal density. Because of the energy factor $(\hbar\omega)^2$ in Eq. (3), this also very slightly changes the absolute magnitude of the x-ray absorption. Although the shifts of the x-ray edges due to changes in the single-particle energies can easily be calculated (see Table IV), the pressure dependence of the core-hole relaxation shift is not known, and we therefore also used the same (normal-density) binding energies[77] for the high-pressure calculations. The x-ray spectra can easily be scaled for shifts in the edge positions if better high-pressure values become available.

Because of the finite lifetime of the excited core hole and ejected electron, the initial spectra, which are calculated assuming sharp initial and final states, must be broadened as shown in Eq. (7). At normal density, the core-hole lifetime can be estimated from either atomic calculations or experimental evidence. Since there is no knowledge about the pressure dependence currently available, we have used the atomic core-hole lifetimes[50–55] for our high-pressure calculations (cf. Table III). For the excited-state widths $\Gamma_x(E)$, we have used Eq. (8) Strictly speaking, the velocity $v_x(E)$ in Eq. (8) should not be zero at E_F. However, given the uncertainties in $\lambda_x(E)$, the use of a free-electron form for v_x, and the rough insensitivity of Γ_x to the zero of energy for v_x, we have forced v_x to zero at E_F to guarantee that Γ_x goes properly to zero at E_F. Electron-gas results[58,78] in the random-phase approximation (RPA) suggest that, for energies well above E_F, where the fundamental damping mechanism is plasmon excitations, Γ_x will increase slowly with density, while at lower energies, where electron-electron scattering dominates, Γ_x will increase more rapidly (roughly as $r_s^{-3/2}$). However, given the uncertainties in application of the RPA calculations to real metals, we have used the normal-density $\Gamma_x(E)$ for all densities.

Another concern about our calculations involves the use of a ground-state potential for excited states, which should "see" a different exchange-correlation potential than low-lying states. The inclusion of these self-energy effects,[79,80] which also may have a pressure dependence, is beyond the scope of this work, although it should be easy to generalize the method to handle energy-dependent potentials. We also point out that all our calculations are done in the dipole approximation. Quadrupole and higher-order corrections should be small[11] for a low-Z material such as copper, and, in any case, should be relatively structureless.

In order to experimentally achieve high compressions, some techniques introduce large amounts of heating and hence strong thermal disorder. These effects, which would introduce additional broadening, are not included in our calculations. They are more naturally introduced within an EXAFS formalism through Debye-Waller factors[81] instead of in a band-structure formalism. By extending the EXAFS formulation to the case of liquids, perhaps through the use of pair-distribution functions, in the future it may be possible to realistically include these effects even for strongly shocked systems that undergo melting. As we have mentioned in the Introduction, we believe that our present calculations are more appropriate for isentropic and diamond-anvil compression techniques for which the Debye-Waller factor would actually decrease with compression.[19]

Finally, the x-ray-absorption calculations presented here suggest that one could use the shift of the energy positions of peaks relative to the x-ray-absorption edge as a simple diagnostic tool to determine the density of materials under pressure, and hence the pressure itself from Table I, depending on the mode of compression. The $V^{-2/3}$ scaling that we are about to describe may seem obvious from the appearance of $ES^2 \approx EV^{2/3}$ in Eq. (11); however, we note that the phase shifts δ_l that appear in Eq. (11), both explicitly and through $f(\pi)/S$, do *not*, in general, scale on volume in this manner. Thus our observations are a true result of the present calculations and compliment those already documented for comparing different materials at 1 atm.[9–13]

In Table VI we show how well various peaks scale with $V^{-2/3}$. For the most part, the peaks follow the scaling relation reasonably closely. The worst case is peak D, which sits at $x=77.8$ at $V_0/V=1$ and slowly increases to $x=88.7$ by the time $V_0/V=10$, a 14% increase in x. Part of this increase is probably a mistake in identification between $V_0/V=1$ and 2. Because the scattering amplitude is changing as a function of energy as well as function of compression, the relative size of x-ray-absorption structure also changes. At $V_0/V=1$, peak D probably contains a weak substructure, which is washed out by the broadening. By the time $V_0/V=2$, the scattering amplitude is much stronger and the substructure starts to become observable and distort relative to $V_0/V=1$. If we assume that the substructure in peak D has started to

TABLE VI. Scaled position, i.e., $S^2(E-E_F)$, of the K-edge x-ray-absorption peaks of Cu as a function of compression. The peaks labeled $A-D$ correspond to those shown in Fig. 5.

	Position of peaks for K edge			
V_0/V	A	B	C	D
1	23.2	46.9	68.2	77.8
1.3	22.9	46.7	68.5	81.1
2	22.7	47.0	68.5	84.5
3	23.6	49.3	68.2	85.9
5	23.5	51.7	67.5	87.8
7	25.2	51.4	66.4	88.0
10	25.5	51.2	67.7	88.7

resolve into several features, and the relative size of features is changing as a function of compression, then it becomes reasonable that the "shoulder" between peaks C and D at $V_0/V=2$ might correspond to peak D at $V_0/V=1$. If we make this assumption and ignore the comparison between $V_0/V=1$ and 2, then the relative increase in the peak position as a function of x then only increases by about 8% between $V_0/V=2$ and 10.

If we examine Table VI we find a 10% or less maximum variation in x of the peak positions of $A-C$ over the entire range of compressions up to $V_0/V=10$. Between $V_0/V=1$ and 2 the variation in these peaks is less than 1%. Since this is the region easily accessible experimentally, the energy dependence of the x-ray absorption might indeed serve as a quite accurate density or volume diagnostic.

The virtue of this kind of diagnostic is that the elaborate calculations presented in this paper are unnecessary to determine the density of the compressed material, since the normal-density spectra provide the necessary calibration. For this diagnostic to work correctly the experimentalist need only be careful enough to be sure to follow the same peaks, and that the peaks are above the band-structure-sensitive near-edge region. Moreover, several peaks in the spectra could be used as a diagnostic (since all the peaks in the high-energy range should have the same $V^{-2/3}$ dependence) and cross-checked against each other as a guard against possible broadening problems or mistakes in identifying corresponding peaks. This crosscheck might also aid as a rough first estimate of the accuracy of the density determination made by this procedure.

ACKNOWLEDGMENTS

We thank N. del Grande, W. L. Schaich, J. H. Scofield, J. W. Wilkins, and A. Zangwill for useful conversations on this work. One of us (A.K.M.) would like to thank R. More for pointing out the role played by the Friedel sum in the continuum-lowered free-electron density of states. Part of this work was performed under the auspices of the U.S. Department of Energy by Los Alamos and Lawrence Livermore National Laboratories under Contracts No. W-7405-Eng-36 and No. W-74005-Eng-48.

[1]R. Ingalls, G. A. Garcia, and E. A. Stern, Phys. Rev. Lett. **40**, 334 (1973).

[2]R. Ingalls, E. D. Crozier, J. E. Whitmore, A. J. Seary, and J. M. Tranquada, J. Appl. Phys. **51**, 3158 (1980).

[3]R. Ingalls, J. M. Tranquada, J. E. Whitmore, E. D. Crozier, and A. J. Seary, in *EXAFS Spectroscopy,* edited by B. K. Teo and D. C. Joy (Plenum, New York, 1981), p. 127.

[4]R. Ingalls, J. M. Tranquada, J. E. Whitmore, and E. D. Crozier, in *Physics of Solids Under High Pressure,* edited by J. S. Schilling and R. N. Shelton (North-Holland, Amsterdam, 1981), p. 67.

[5]K. Syassen, G. Wortman, J. Feldhaus, K. H. Frank, and G. Kaindl, in *Physics of Solid Under High Pressure,* Ref. 4, p. 319.

[6]See, e.g., A. Jayaraman, Rev. Mod. Phys. **55**, 65 (1983).

[7]D. K. Bradley, J. D. Hares, J. D. Kilkenny, A. Rankin, and N. C. Holmes, Annual Report to the Laser Facility Committee, 1983, Rutherford Appleton Laboratory Report No. RL-83-043 (unpublished); R. W. Eason, D. K. Bradley, J. D. Kilkenny, and G. N. Greaves (unpublished). In this approach, the sample is surfaced with a thin layer of high-Z material on the side facing the laser. The incident laser pulse not only creates a shock wave that compresses the sample, but, by heating the high-Z layer, also creates a continuum x-ray source in the region of the sample K edge.

[8]See, e.g., J. H. Nuckolls, Phys. Today **35**, (8), 24 (1982); Laser Program Annual Report—1981, Report No. UCRL-50021-81 (Lawrence Livermore National Laboratory, Livermore, CA, 1982) (unpublished).

[9]J. E. Müller, O. Jepsen, O. K. Andersen, and J. W. Wilkins, Phys. Rev. Lett. **40**, 720 (1978).

[10]J. E. Müller, O. Jepsen, and J. W. Wilkins, Solid State Commun. **42**, 365 (1982).

[11]J. E. Müller, Ph.D. thesis, Cornell University, 1980; J. E. Müller and J. W. Wilkins, Phys. Rev. B **29**, 4331 (1984).

[12]G. Materlik, J. E. Müller, and J. W. Wilkins, Phys. Rev. Lett. **50**, 267, (1983).

[13]L. A. Grunes, Phys. Rev. B **27**, 2111 (1983).

[14]For a recent review, see P. A. Lee, P. H. Citrin, P. Eisenberger, and B. M. Kincaid, Rev. Mod. Phys. **53**, 769 (1981).

[15]W. W. Beeman and H. Friedman, Phys. Rev. **56**, 392 (1939).

[16]N. Kerr Del Grande and A. J. Oliver, in *Proceedings of International Symposium on X-Ray Spectra and Electronic Structure of Matter,* edited by A. Faessler and G. Weich (Fotodruck Frank OHG, München, West Germany, 1973).

[17]E. A. Stern, Phys. Rev. B **10**, 3027 (1974); G. Martens, P. Rabe, N. Schwenter and A. Werner, *ibid.* **17**, 1481 (1978); S. I. Salen and V. L. Hall, J. Phys. F **10**, 1627 (1980); G. Vlaic, J. C. J. Bart, and W. Cavigiolo, Chem. Phys. Lett. **76**, 453 (1980); P. Eisenberger and B. Lengler, Phys. Rev. B **22**, 3551 (1980).

[18]G. N. Greaves, P. J. Durham, G. Diakun, and P. Quinn, Nature (London) **294**, 139 (1981).

[19]In the context of a high-temperature Debye model, the isentrope temperature $T_1(V)$ will increase in proportion to the Debye temperature $\Theta_D(V)$ as the volume is reduced. The exponent of the Debye-Waller factor is proportional to $V^{-2/3}T/\Theta_D^2$ [see, e.g., J. M Ziman, *Principles of the Theory of Solids* (Cambridge University Press, Cambridge, 1964)], and will decrease in magnitude under isentropic compression if the Grüneisen parameter $\gamma=-d\ln\Theta_D/d\ln V>\frac{2}{3}$, which is the case for Cu throughout the range of interest in this work.

[20]R. S. Hawke, D. E. Duerre, J. G. Huebel, H. Klapper, D. J. Steinberg, and R. N. Keeler, J. Appl. Phys. **43**, 2734 (1972).

[21]See, e.g., L. M. Barker, in *Shock Waves in Condensed Matter—1983,* edited by J. R. Assay, R. A. Graham, and G. K. Straub (North-Holland, Amsterdam, 1984).

[22]J. Nuckolls, L. Wood, A. Thiessen, and G. Zimmerman, Nature (London) **239**, 139 (1972).

[23]S. Jackel, D. Salzmann, A. Krumbein, and S. Eliezer, Phys. Fluids **26**, 3138 (1983).

[24]T. L. Loucks, *Augmented Plane Wave Method* (Benjamin,

New York, 1967); L. F. Mattheiss, J. H. Wood, and A. C. Switendick in *Methods in Computational Physics,* edited by B. Adler, S. Fernback, and M. Rotenberg (Academic, New York, 1968), Vol. 8, p. 63.

[25]See. e.g., M. Ross and K. W. Johnson, Phys. Rev. B **2**, 4709 (1970); A. K. McMahan and M. Ross, Phys. Rev. **15**, 718 (1977).

[26]L. Hedin and B. I. Lundqvist, J. Phys. C **4**, 2064 (1971).

[27]O. K. Andersen, Phys. Rev. B **12**, 3060 (1975); O. K. Andersen and O. Jepsen, Physica (Utrecht) **91B**, 317 (1977).

[28]H. L. Skriver, *The LMTO Method, Muffin-Tin Orbitals and Electron Structure* (Springer, Berlin, 1984).

[29]A modification of the program described in Ref. 28 was used, which included self-consistent treatment of the core, and is described in A. K. McMahan, H. L. Skriver, and B. Johansson [Phys. Rev. B **23**, 5016 (1981)].

[30]U. von Barth and L. Hedin, J. Phys. C **5**, 1629 (1972).

[31]A. K. McMahan and R. C. Albers, Phys. Rev. Lett. **49**, 1198 (1982). Since this paper was published, the authors were informed of an earlier prediction that Ni would become insulating at very high pressure: G. M. Gandel'man, V. M. Ermachenko, and Ya. B. Zel'dovich, Zh. Eksp. Teor. Fiz. **44**, 386 (1963) [Sov. Phys.—JETP **17**, 263 (1963)].

[32]D. Glötzel and O. K. Andersen (unpublished); see also D. Glötzel and A. K. McMahan, Phys. Rev. B **20**, 3210 (1979).

[33]E. Esposito, A. E. Carlsson, D. D. Ling, H. Ehrenreich, and C. D. Gelatt, Jr., Philos. Mag. A **251**, (1980).

[34]J. F. Janak, Phys. Rev. B **9**, 3985 (1974).

[35]F. D. Murnaghan, Proc. Nat. Acad. Sci. U.S.A. **30**, 244 (1944).

[36]V. I. Moruzzi, J. F. Janak, and A. R. Williams, *Calculated Electronic Properties of Metals* (Pergamon, New York, 1978).

[37]*American Institute of Physics Handbook,* 3rd ed. (McGraw-Hill, New York, 1970), Table 9d-3; *Physical Acoustics,* edited by W. P. Mason (Academic, New York, 1965), Vol. III B, Appendix 1.

[38]D. Glötzel, in *Physics of Solids under Pressure,* Ref. 4, p. 268 (Fig. 2).

[39]H. K. Mao, P. M. Bell, J. W. Shaner, and D. J. Steinberg, J. Appl. Phys. **49**, 3276 (1978).

[40]W. J. Carter, S. P. Marsh, J. N. Fritz, and R. G. McQueen, in *Accurate Characterization of the High-Pressure Environment,* Nat. Bur. Stand. (U.S.) Spec. Pub. No. 326 (U.S. GPO, Washington, D.C., 1971), p. 147.

[41]Based on a Debye model and the volume-dependent, low-temperature Grüneisen parameter used in Ref. 43.

[42]A. C. Mitchell and W. J. Nellis, J. Appl. Phys. **52**, 3363 (1981).

[43]K. S. Trainor, J. Appl. Phys. **54**, 2372 (1983). This paper describes the assembly of an equation of state for Cu, which includes, among other contributions, the $T=0$ APW results reported in the present work.

[44]Rydberg atomic units are used throughout the present paper ($e^2=2$, $\hbar=1$, and $m=\frac{1}{2}$). The dimensionless energy ES^2 is thus $E(2mS^2/\hbar^2)$.

[45]J. Friedel, Adv. Phys. **3**, 446 (1954); C. Kittel, *Quantum Theory of Solids* (Wiley, New York, 1963).

[46]P. W. Anderson and W. McMillan, in *Theory of Magnetism in Transitional Metals, Course 37* (Academic, New York, 1967); R. M. More and K. Hacker, Phys. Rev. B **2**, 3039 (1970).

[47]See. e.g., K. Gottfried, *Quantum Mechanics* (Benjamin, New York, 1966), Vol. I, p. 394.

[48]L. I. Schiff, *Quantum Mechanics,* 2nd ed. (McGraw-Hill, New York, 1955), p. 167.

[49]This description of the method for calculating the x-ray-absorption coefficient has already been given in Ref. 10 and is repeated here for clarity.

[50]W. Bambynek *et al.*, Rev. Mod. Phys. **44**, 716 (1972).

[51]O. Keski-Rahkonen and M. O. Krause, At. Data Nucl. Data Tables **14**, 139 (1974).

[52]J. H. Scofield, At. Data and Nucl. Data Tables **14**, 121 (1974).

[53]E. J. McGuire, Phys. Rev. A **3**, 587 (1971).

[54]E. J. McGuire, Phys. Rev. A **3**, 1801 (1971).

[55]L. I. Yin, I. Adler, M. H. Chen, and B. Crasemann, Phys. Rev. A **7**, 897 (1973).

[56]I. Lindau and W. Spicer, J. Electron Spectrosc. Relat. Phenom. **3**, 409 (1974).

[57]W. Gudat (private communication).

[58]J. J. Quinn, Phys. Rev. **126**, 1453 (1962).

[59]We distinguish between overall magnitude and the size of the peaks and the valleys in the structure of the spectra. The latter grows quite dramatically with pressure in some energy regions. By overall magnitude we mean the rough average level of absorption that the structure oscillates about.

[60]J. H. Hubbel *et al.*, in *X-Ray Cross Sections and Attenuation Coefficients, International Tables for X-Ray Crystallography,* edited by J. A. Ibers and W. C. Hamilton (Kynoch, Birmingham, 1974), Vol. IV. Sec. 2.1.

[61]J. H. Scofield (private communication).

[62]G. D. Mahan, in *Solid State Physics,* edited by H. Ehrenreich, F. Seitz, and D. Turnbull (Academic, New York, 1974), Vol. 29.

[63]U. Fano and J. W. Cooper, Rev. Mod. Phys. **40**, 441 (1968).

[64]The x-ray absorption at the edge is due to excitations that just have enough energy to excite a core electron into the unoccupied states just above the Fermi energy.

[65]J. E. Müller and W. L. Schaich, Phys. Rev. B **27**, 6489 (1983).

[66]R. C. Albers and J. J. Rehr (unpublished).

[67]F. Bechstedt, Phys. Status Solidi B **112**, 9 (1982); A. Rosen and I. Lindgren, Phys. Rev. **176**, 114 (1968).

[68]L. Hedin and A. Johansson, J. Phys. B **2**, 1336 (1969).

[69]D. A. Shirley, Chem. Phys. Lett. **16**, 220 (1972).

[70]R. E. Watson, M. L. Perlman, and J. F. Herbst, Phys. Rev. B **13**, 2358 (1976).

[71]K. Schwarz, J. Phys. B **11**, 1339 (1978).

[72]U. von Barth and G. Grossman, Solid State Commun. **32**, 645 (1979).

[73]U. von Barth and G. Grossman, Phys. Scr. **21**, 580 (1980).

[74]G. D. Mahan, Phys. Rev. B **21**, 1421 (1980).

[75]L. C. Davis and L. A. Feldkamp, Phys. Rev. B **23**, 4269 (1981).

[76]U. von Barth and G. Grossman, Phys. Rev. B **25**, 5150 (1982).

[77]The experimental positions of all edges, except L_1, were taken from Table VI of J. A. Bearden, Rev. Mod. Phys. **39**, 78 (1967). The L_1 value is from Table I of J. A. Bearden and A. F. Burr, Rev. Mod. Phys. **39**, 125 (1967).

[78]B. I. Lundqvist, Phys. Status Solidi **32**, 273 (1969).

[79]L. Hedin and B. I. Lundqvist, J. Phys. C **4**, 2064 (1971).

[80]R. E. Watson, J. F. Herbst, L. Hodges, B. I. Lundqvist, and J. W. Wilkins, Phys. Rev. B **13**, 1463 (1976).

[81]P. P. Lottici and J. J. Rehr, Solid State Commun. **35**, 565 (1980).